Robust Thermal Bias Estimation in Real-World Infrared Images Via Integrating Outlier Suppression and Second-Order ℓ_0 Norm Sparsity

Li Liu, *Member, IEEE*, Ji Liu, Xinchao Zhang, Weihua Meng, and Houzhang Fang, *Member, IEEE*

***Abstract*—Removing the complex thermal bias from real-world infrared (IR) images degraded by thermal radiation effects is significantly crucial to improving image quality of high-precision IR cameras. Traditional IR image correction methods always neglect the impact of both unavoidable interference and salient image structures not to produce a high-contrast correction image. In this study, a robust and efficient thermal bias estimation method is proposed to compensate the complicated nonuniformity in noisy IR images. Specifically, the suppression strategy of outliers and salient structures is successfully made to significantly improve the estimation precision on the basis of the salient gradient difference between thermal bias and image structures. Meanwhile, the second-order ℓ_0 norm sparsity in gradient domain helps not only to avoid the staircase effects, but also effectively suppress system noise. The experimental results on real-world infrared datasets demonstrate the superiority of the proposed method over existing correction methods in terms of both correction residuals and visual quality.**

***Index Terms*—Image correction, infrared (IR) nonuniformity, outlier suppression, second-order gradient sparsity.**

I. Introduction

INFRARED (IR) imaging systems have been widely used in a variety of fields, such as remote sensing, astronomy imaging, celestial navigation, and video surveillance, leveraging their excellent ability to detect temperature variations and visualize IR patterns. However, temperature fluctuations of optical lens and other mechanical components in the interior of IR imaging systems will cause a global smooth thermal bias in captured images [1], [2], severely degrading image quality and affecting the subsequent target detection and recognition. Since the temperature of optical lens significantly increases in severe thermal environment, removing the spatially temporally variant thermal bias is challenging. Meanwhile, hybrid noises from an IR detector inevitably affect estimation accuracy. Thus, robust estimation of thermal bias from severely degraded IR images is crucial to improving the performance of IR imaging systems.

A. Related Works

Thermal bias correction has aroused widespread interests in both industrial and academic fields, and many novel correction methods have been proposed to make a great success in practical applications. In a nutshell, these new techniques can be broadly classified into three classes: 1) surface fitting; 2) deep learning; 3) variational optimization.

1) Surface Fitting-Based Methods: Restrepo-Girón and Loaiza-Correa [3] applied median filtering with a decimated kernel to decouple the background thermal bias from IR images with defective areas. Then, Zhang et al. [4] used a second-order polynomial curve-fitting model to estimate the nonuniform background from thermal data with nondefective area. Cao and Tisse [5] employed an optimized bilateral filter to remove image details and noise, and subsequently estimated the parameters of a bivariate polynomial fitting model in image gradient domain. Although the bilateral filter can remove trivial image textures and suppress noise, the image correction method integrated with it has relatively low computational efficiency, limiting its practical application. Similarly, Li et al. [6] designed a multiframe correction framework to estimate the interior radiation noise. Different from the bivariate polynomial function, the authors in [7] and [8] introduced the Chebyshev and Bézier polynomial surface fitting methods to estimate thermal radiation bias. Recently, Xie et al. [9] has improved the correction robustness by applying the Huber function with an adaptive threshold to limit the impact of salient structures. Liu et al. [10] has proposed an enhanced least mean square method to estimate thermal bias in image gradient domain. Although the surface fitting-based correction methods can improve estimation accuracy, their correction performance may be affected by both salient structures and mixed noise.

Received 29 April 2025; revised 28 August 2025 and 25 September 2025; accepted 13 October 2025. Date of publication 15 October 2025; date of current version 29 October 2025. This work was supported in part by the Aeronautical Science Foundation under Grant ASFC-20240001081002, in part by the Open Research Fund of the National Key Laboratory of Multispectral Information Intelligent Processing Technology under Grant 61421132301, in part by the National Natural Science Foundation of China under Grant 62371375, and in part by the Innovation Capability Support Program of Shaanxi under Grant 2022TD37. *(Corresponding author: Li Liu.)*

Li Liu is with the School of Aerospace Science and Technology, Xidian University, Xi'an 710126, China (e-mail: dr.liliu@hotmail.com).

Ji Liu is with China Academy of Space Technology, Xi'an 710000, China (e-mail: liuji@stu.xidian.edu.cn).

Xinchao Zhang is with the School of Computer and Artificial Intelligence, Zhengzhou University, Zhengzhou 450001, China, and also with the National Key Laboratory of Air-based Information Perception and Fusion, Luoyang 471009, China (e-mail: drxinchaozhang@gmail.com).

Weihua Meng is with the National Key Laboratory of Air-based Information Perception and Fusion, Luoyang 471009, China (e-mail: drweihuameng@gmail.com).

Houzhang Fang is with the School of Computer Science and Technology, Xidian University, Xi'an 710126, China (e-mail: houzhangfang@xidian.edu.cn).

Digital Object Identifier 10.1109/JSTARS.2025.3622142

© 2025 The Authors. This work is licensed under a Creative Commons Attribution-NonCommercial-NoDerivatives 4.0 License. For more information, see https://creativecommons.org/licenses/by-nc-nd/4.0/

2) Deep Learning-Based Methods: With the significant advancements of deep learning in image restoration, researchers have gradually pushed forward deep learning-based correction methods. For example, a creative correction model can simultaneously estimate thermal bias and stripe noise by introducing residual learning strategies and multiscale networks [11]. Despite achieving good results on simulated datasets, its performance is often hindered due to the complexity of the degradation process in the real world. Recently, Shi et al. [12] designed a semi-supervised learning network for thermal radiation correction to improve the robustness in the real-world images, and proposed a surface fitting constrained multidimensional hybrid attention aero-optics thermal radiation correction network [13]. Fang et al. [14] proposed a detection-friendly union framework, that simultaneously addressed both infrared NUC and UAV target detection tasks in an end-to-end manner. Although these new learning-based methods can achieve the good performance in some cases, it is difficult to generalize such networks to the real-world images outside the training datasets due to the diversity of captured images and the complexity of IR nonuniformity from image acquisition. One solvable correction strategy is to combine physics-inspired model with learning-based model in order to leverage their respective merits to effectively improve the correction performance especially for real-world images. The integration of physical modeling with deep network-based image representation has been applied to separate a sequence of images into the scene-dependent radiant flux, and a slowly changing scene-independent nonuniformity without much training data [15]. However, thermal radiation effects in real-world images are often more severe and complex than that in [15]. In addition, mixed noise from the real world significantly affects the correction performance of learning-based model.

3) Variational Optimization-Based Methods: Inspired by Retinex-based image enhancement [16], the variational correction framework has been developed to separate the additive thermal bias from the degraded IR image. For example, we proposed a thermal radiation image correction model based on ℓ_0 norm regularization [17]. Its advantage is that simultaneous thermal bias estimation and denoising can be conducted in a unified variational framework. However, its disadvantage is that the estimated thermal bias may be affected by high-contrast structures, and meanwhile the staircase effects could happen in the process of denoising. Wang et al. [18] proposed a contrast enhancement method based on cyclic multiscale illumination self-similarity and gradient perception regularization to remove thermal bias. This kind of image correction strategy neglects the impact from image salient structures and mixed noise on correction precision. For simultaneous thermal bias correction and destriping in [19], a bivariate polynomial model was used to characterize the global smoothness of thermal bias, and was integrated into one unified variational model to effectively improve the quality of real-world IR images. Recently, Liu et al. [20] separated low-frequency thermal bias from the scene by using Fourier transform. He et al. [21] introduced frequency-domain priors in a plug-and play framework, which were beneficial for joint stripe removal and thermal bias estimation. However, salient image structures and outliers could have an important impact on correction accuracy. Thus, for real-world IR images with salient edges or outliers, the performance of the abovementioned methods may significantly degrade.

B. Challenges and Motivations

When an IR scene with complex thermal bias has outliers, such as dead pixels, impulsive noise, and saturated pixels, how to handle these outliers is crucially important in improving the estimation precision of thermal bias. Traditional image restoration methods have introduced elaborate data fidelity terms in order to suppress the influence of outliers. For example, the Huber's M-estimator was adopted to suppress the influence of outliers in blind image deblurring [22]. The saturated pixel handling schemes in [23] made the nonblind deblurring method robust to different saturation levels. However, the impact of outliers on thermal bias estimation in IR scenes has not been emphasized in [9], [13], [14], and [24]. In practical applications, the original IR scenes are degraded by thermal bias superimposed with saturated pixels and mixed noises, and thus it is much challenging to accurately estimate the latent thermal bias.

In addition, the salient structures in IR scenes have also an important impact on estimation precision, such as edges, sea–sky lines, river banks, and so on. How to maintain the sharp contrast of an IR scene in the process of estimating the large-scale thermal bias is significant. Recently, the adaptive correction method in [9] has considered the impact of image content on thermal bias, which applied Huber function-based loss that flexibly switched between the ℓ_1 and ℓ_2 norms for the different regions of the degraded image. However the low-order bivariate polynomial surface model cannot well fit the thermal bias from real-world degraded images. Meanwhile, the variation of IR scenes and mixed noise may degrade its performance. For example, the IR background in Fig. 1(a) is severely degraded by both large-scale thermal bias and outlier pixels in the leftmost column and the sky–sea line has the highest contrast in the whole IR scene. Simultaneous thermal bias estimation and structure preservation must be comprehensively considered in a unified correction framework. The proposed method can produce a sharp contrast-preserving resulting image in Fig. 1(b) by effectively removing the thermal bias in Fig. 1(c). The different image patches cropped from Fig. 1(a) and (b), respectively, are shown in Fig. 1(d).

In this study, the correction performance of the proposed method is improved from the following aspects. First, the high-order bivariate polynomial function is used to characterize the global smoothness of the complex thermal bias due to its high robustness. Second, the outlier handling scheme is elaborately designed in order to limit the impact of both outliers and high-contrast structures on thermal bias estimation. Finally, the second-order ℓ_0 norm sparsity in image gradient domain helps not only to avoid the staircase effects but also to suppress the random noise from the original image. Thus, a clear contrast-preserving corrected image can be obtained, which provides a great advantage for subsequent high-level image tasks.

The rest of this article is organized as follows. In Section II, we discuss the basic principles of simultaneous thermal bias

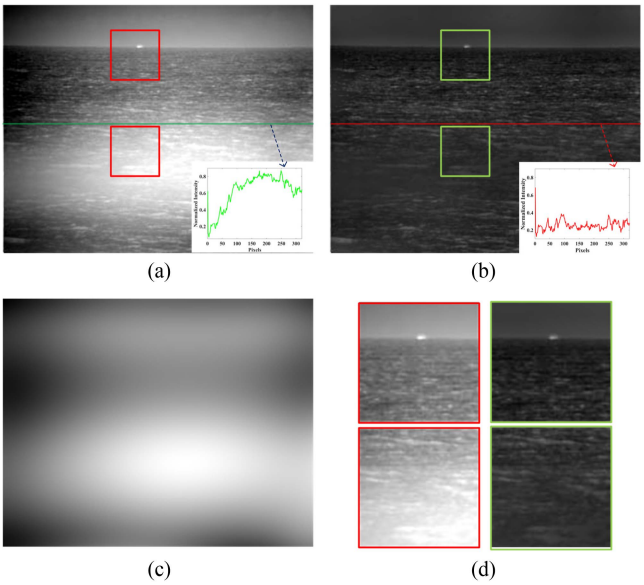


Fig. 1. (a) Real IR image degraded by thermal nonuniformity and outlier pixels in the leftmost column. (b) Corrected IR image. (c) Estimated thermal bias from (a). (d) Image patches cropped from (a) and (b). A line of normalized intensities from (a) and (b), respectively is shown in the southeast.

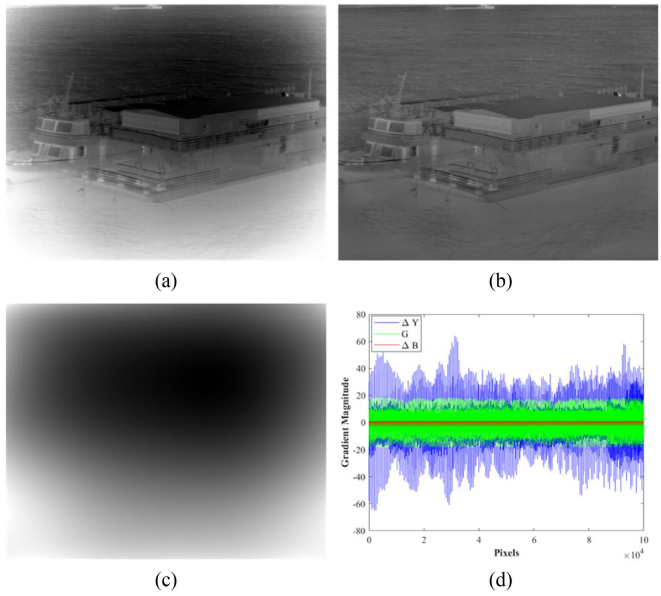


Fig. 2. (a) Degraded IR image. (b) Corrected image. (c) Estimated thermal bias from (a). (d) Vectorized gradient ∇Y, guide gradient G, and thermal bias gradient ∇B (σ =1, ϵ =10).

estimation and noise removal and apply the HQ solver to solve the correction model. And we analyze the experimental results in Section III. Finally, Section IV concludes this article.

II. Simultaneous Thermal Bias Estimation and Denoising

A. Robust Thermal Bias Correction

Generally, thermal bias is induced by thermal radiation effects of IR background, such as heated optical lens and temperature fluctuations of background. Thus, the image degradation process can be expressed by a simple linear model as follows:

$$\mathbf{Y} = \mathbf{I} + \mathbf{B} + \xi \tag{1}$$

where $\mathbf{Y}$, $\mathbf{I}$, and $\mathbf{B}$ are the degraded IR image, the latent sharp IR image, and thermal bias, respectively, and ξ denotes system noise. It is much challenging to accurately estimate the additive thermal bias $\mathbf{B}$ from the severely degraded IR image $\mathbf{Y}$, especially when the latent IR $\mathbf{I}$ contains high-contrast structures and the system noise ξ is complex. In this study, the proposed correction model is optimized from three aspects in order to improve its robustness in a complex noisy environment: 1) parametric thermal bias modeling; (2) outlier and salient structure suppression; (3) second-order ℓ_0 norm sparsity in gradient domain.

1) Parametric Thermal Bias Modeling: Since IR images inevitably contain mixed noises, and in some cases have saturated pixels, the parametric thermal bias model has the great advantage over the nonparametric one. First, the parametric thermal bias model can effectively express the complex characteristics of thermal biases from real-world IR scenes. Second, it is robust to outliers and random noise. Thus, the parametric thermal bias can be expressed as follows:

$$\mathbf{B} = \sum_{t=0}^{K}\sum_{s=0}^{K-t} a_{t,s} x^t y^s = \mathbf{W}\mathbf{a} \tag{2}$$

where $\mathbf{W}$ denotes the row vectors holding the monomial terms, and $\mathbf{a}$ is the column vector form of $a_{t,s}$ and its corresponding derivative version can also be expressed as a linear combination of model parameters $\mathbf{a}$

$$\begin{aligned}\nabla_{\mathbf{x}}\mathbf{B} &= \sum_{t=0}^{K}\sum_{s=0}^{K-t} a_{t,s}\left(x^t - x_r^t\right) y^s = \mathbf{C}_{\mathbf{x}}\mathbf{a} \\ \nabla_{\mathbf{y}}\mathbf{B} &= \sum_{t=0}^{K}\sum_{s=0}^{K-t} a_{t,s} x^t \left(y^s - y_r^s\right) = \mathbf{C}_{\mathbf{y}}\mathbf{a}\end{aligned} \tag{3}$$

where ∇ denotes the gradient operator, and $\mathbf{C}$ is similar with $\mathbf{W}$.

2) Outlier and Salient Structure Suppression: How to suppress the impact of both outliers and high-contrast image structures on estimation accuracy is significantly important. It has been demonstrated that parametric bias correction has the superiority for noisy IR images due to its excellent global modeling of thermal bias [17]. However, its performance may be limited by the outliers or high-contrast IR structures. Thus, it is necessary to make the successful suppression strategy in order to improve the robustness of IR image correction further.

Since the gradient difference between outliers, salient IR structures, and thermal bias shown in Fig. 2(d) is significant, it is workable to improve the estimation accuracy by limiting the gradients of degraded IR images. Specifically, the guide gradient map $\mathbf{G}$ is designed as the constrained version of $\nabla\mathbf{Y}$, where ∇ denotes the first-order gradient operator. And the formulation of

$\mathbf{G}$ is expressed as follows:

$$\mathbf{G} = \mathbf{R} \circ \nabla \mathbf{Y}$$
$$\mathbf{R} = \begin{cases} e^{(-|\nabla \mathbf{Y}|/\sigma)}, & |\nabla \mathbf{Y}| > \epsilon \\ 1, & |\nabla \mathbf{Y}| < \epsilon \end{cases} \tag{4}$$

where $\circ$ denotes element-wise multiplication. The factor $\mathbf{R}$ can directly control the gradient magnitude of $\mathbf{G}$. The bigger the degraded image gradient $\nabla \mathbf{Y}$ is, the smaller the factor $\mathbf{R}$ is. Since the gradient magnitudes of thermal bias are not large, the small gradient components in $\nabla \mathbf{Y}$ are not affected. After the reduction, the factor $\mathbf{R}$ can effectively weaken the impact of the gradients of both outliers and salient structures on the thermal bias. Further, σ controls the reduction rate of high gradient magnitude. ϵ is the threshold value of image gradient. As σ and ϵ are set to 1 and 10, respectively, the comparison of vectorized gradient ∇Y, guide gradient G, and thermal bias gradient ∇B is shown in Fig. 2(d).

Thus, we propose a new optimization function to simultaneously estimate the latent IR image $\mathbf{I}$ and thermal bias $\mathbf{B}$ from the degraded image $\mathbf{Y}$:

$$\min \|\mathbf{Y} - \mathbf{I} - \mathbf{B}\|_2^2 + \alpha \|\mathbf{G} - \nabla \mathbf{B}\|_1 \tag{5}$$

where α is the weight for balance. The first term is data fidelity, and the second term aims to suppress the impact of high gradient magnitudes on thermal bias. $\|\cdot\|_1$ denotes the ℓ_1 norm.

3) Second-Order ℓ_0 Norm Sparsity in Image Gradient Domain: The latent thermal bias cannot be accurately estimated only with the optimization model (5). Since the real-world degraded IR images unavoidably contain complex mixed noise, how to effectively remove system noise and preserve salient edges and corners is a core issue in the process of estimating thermal bias. Previous study has demonstrated that the well-designed regularization models can significantly suppress system noise in image restoration methods, such as deep plug-and-play priors [21], hybrid low-rank and sparsity constraint [25], [26], group sparsity [27], and illumination channel sparsity [28]. In addition, higher order regularization has been applied to improve the performance [29], [30], [31], [32]. For example, a generalized total variational denoising model in [29] was used to well preserve detail information and similarly the integration of high-order total variation and ℓ0-norm wavelet frame helps to avoid the staircase artifacts [30]. Although these higher order methods deliver high-quality performance, they typically involve solving an optimization problem, that is computationally intensive for large-scale data samples in practice.

As for IR nonuniformity correction, the estimation precision of complex thermal bias depends closely on both noise suppression and salient structure preservation during the solving process. Despite the success of ℓ_0 norm regularization in thermal bias estimation [17], it may fail in image regions where sparse prior constraints are not satisfied, especially in slanted areas. It can be easily demonstrated that first-order image gradients in the slanted areas are not fully sparse because their values are larger than zero. As a result, the staircase effects will be induced when directly imposing the first-order gradient regularization. Obviously, the nonzero elements of first-order gradient $\nabla \mathbf{I}$ are not fully sparse but concentrated in slanted areas. In contrast, the second-order gradient $\Delta \mathbf{I}$ is sparse within these same regions. Thus, $\nabla \mathbf{I}$ and $\Delta \mathbf{I}$ can satisfy

$$\begin{cases} \|\nabla \mathbf{I}\|_0 > N \\ \|\Delta \mathbf{I}\|_0 < M \end{cases} \tag{6}$$

where N and M are positive integers satisfying $N \gg M$. The benefit of (6) is straightforward: the nonzero entries of $\Delta \mathbf{I}$ are significantly fewer than that of $\nabla \mathbf{I}$, meaning $\Delta \mathbf{I}$ is inherently sparser than $\nabla \mathbf{I}$. This observation motivates us to introduce the second-order sparse prior for excellent performance.

In a nutshell, the parametric correction model has the great advantage especially in noisy environment, and the integration of outlier handling scheme and second-order ℓ_0 norm sparsity in gradient domain can improve the robustness of the correction model further. Based on the above discussion, the proposed correction model can be expressed as follows:

$$\min \|\mathbf{Y} - \mathbf{I} - \mathbf{W}\mathbf{a}\|_2^2 + \alpha \|\mathbf{G} - \mathbf{C}\mathbf{a}\|_1 + \beta \|\Delta \mathbf{I}\|_0 \tag{7}$$

where β is the model parameter, and Δ denotes the second-order gradient operator in the horizontal, vertical and diagonal directions.

B. Iterative Framework Using Half-Quadratic (HQ) Solver

The optimization problem in (7) can be effectively solved by HQ splitting since it has the fast convergence and superior numerical stability for large-scale problems. To address the ill-posed problem (7), we iteratively estimate the latent IR image $\mathbf{I}$ and the coefficients $\mathbf{a}$ of the parametric thermal bias $\mathbf{B}$. Thus, our model can be split into the following objective subfunctions:

$$\begin{cases} \min \|\mathbf{Y} - \mathbf{I} - \mathbf{W}\mathbf{a}\|_2^2 + \alpha \|\mathbf{G} - \mathbf{C}\mathbf{a}\|_1 & (8) \\ \min \|\mathbf{Y} - \mathbf{I} - \mathbf{W}\mathbf{a}\|_2^2 + \beta \|\Delta \mathbf{I}\|_0 . & (9) \end{cases}$$

1) Estimating the Coefficients $\mathbf{a}$ *With* $\mathbf{I}$*:* The main idea of HQ splitting technique is to introduce an auxiliary variable to split the original problem into sub-problems that can be solved efficiently. By fixing $\mathbf{I}$, one auxiliary variable $\mathbf{T}$ is introduced to substitute $\mathbf{G} - \mathbf{C}\mathbf{a}$ and change (8) to the following optimization problem:

$$\min \|\mathbf{Y} - \mathbf{I} - \mathbf{W}\mathbf{a}\|_2^2 + \alpha \|\mathbf{T}\|_1 + \alpha' \|\mathbf{G} - \mathbf{C}\mathbf{a} - \mathbf{T}\|_2^2 \tag{10}$$

where α' is a penalization parameter. The $\mathbf{a}$-related subproblem is given by

$$\min \|\mathbf{Y} - \mathbf{I} - \mathbf{W}\mathbf{a}\|_2^2 + \alpha' \|\mathbf{G} - \mathbf{C}\mathbf{a} - \mathbf{T}\|_2^2 \tag{11}$$

which is a least-square problem. Thus, its closed-form solution can be computed

$$\mathbf{a} = \mathbf{R}^{-1} \left(\mathbf{W}^T (\mathbf{Y} - \mathbf{I}) + \alpha' \mathbf{C}^T (\mathbf{G} - \mathbf{T}) \right) \tag{12}$$

where $\mathbf{R}$ equals to $\mathbf{W}^T\mathbf{W} + \alpha'\mathbf{C}^T\mathbf{C}$.

Then, the $\mathbf{T}$-related subproblem is

$$\min \alpha \|\mathbf{T}\|_1 + \alpha' \|\mathbf{G} - \mathbf{C}\mathbf{a} - \mathbf{T}\|_2^2 \tag{13}$$

which can be solved by the shrinkage operator as follows:

$$\mathbf{T} = \mathbf{shrinkage} \left(\mathbf{G} - \mathbf{C}\mathbf{a}, \frac{\alpha}{2\alpha'} \right). \tag{14}$$

2) Estimating the Latent $\mathbf{I}$ *With the Parameters* $\mathbf{a}$*:* Minimizing the $\mathbf{I}$-related subproblem (9) can be done in a similar fashion. By introducing another auxiliary variable $\mathbf{S}$, the $\mathbf{I}$-related subproblem can be converted into

$$\min \|\mathbf{Y}-\mathbf{I}-\mathbf{Wa}\|_2^2+\beta\|\mathbf{S}\|_0+\beta'\|\mathbf{S}-\Delta\mathbf{I}\|_2^2 \tag{15}$$

where β' is a penalization parameter.

The latent image $\mathbf{I}$ can be obtained by solving the following subproblem:

$$\min \|\mathbf{Y}-\mathbf{I}-\mathbf{Wa}\|_2^2+\beta'\|\mathbf{S}-\Delta\mathbf{I}\|_2^2 \tag{16}$$

For periodic images, the closed-form solution to this least squares minimization problem is

$$\mathbf{I}=\mathcal{F}^{-1}\left(\frac{\mathcal{F}(\mathbf{Y}-\mathbf{Wa})+\beta'\mathcal{F}(\Delta^T\mathbf{S})}{\mathcal{F}(1)+\beta'\mathcal{F}(\Delta^T\Delta))}\right) \tag{17}$$

where $\mathcal{F}$ and $\mathcal{F}^{-1}$ denotes the FFT and IFFT operators. There are three advantages of solving (16) with (17). First, (17) transforms the inverse of a very large matrix in intensity domain into point-wise divisions in the Fourier domain, which is much faster. Second, only $\mathcal{F}(\mathbf{Wa})$ and $\mathcal{F}(\Delta^T\mathbf{S})$ need to be computed in each iteration, and other constant components can be pre-computed. Third, computing FFT and IFFT in (17) can be highly parallel. Thus, (17) has high efficiency and the $\mathbf{S}$-related subproblem is

$$\min\beta\|\mathbf{S}\|_0+\beta'\|\mathbf{S}-\Delta\mathbf{I}\|_2^2. \tag{18}$$

Note that (18) is a pixel-wise minimization problem, and its solution can be obtained efficiently using a hard-threshold operator [17], [33]

$$\mathbf{S}=\begin{cases}\Delta\mathbf{I}, & ||\Delta\mathbf{I}||_2^2>\frac{\beta}{\beta'}\\ 0, & \text{otherwise.}\end{cases} \tag{19}$$

The above HQ splitting scheme leads to an iterative hard-thresholding algorithm for IR nonuniformity correction, which has several significant advantages. First, it has better convergence rates compared to solving the original nonconvex problem directly. Second, it has high stability and robustness since the iterative framework makes it relatively robust to noise and other imperfections in degraded IR images. Third, it also has wide applicability for high-dimensional data due to its high decomposability. The whole optimization algorithm to solve (7) is summarized in Algorithm 1, where $j_{\max}$ is the maximum iteration number and the stopping criterion of the proposed algorithm is based on the relative change (Relcha) between two successive latent images. The numerical experiment results can demonstrate the effectiveness and efficiency of the proposed correction algorithm.

Algorithm 1: Robust Thermal Bias Estimation Based on HQ Splitting (7).

INPUT: Degraded image $\mathbf{Y}$, parameters α, α', β, β'.
INITIALIZATION: $\mathbf{I}_0=\mathbf{T}_0=\mathbf{S}_0=0$, $\mathbf{G}=\mathbf{R}\circ\nabla\mathbf{Y}$, $r=\sqrt{2}$, $\xi=0.0001$, $j_{max}=50$.
While *Relcha* $>\xi$ and $j<j_{max}$
Update $\mathbf{a}_{j+1}$, via (12);
Update $\mathbf{T}_{j+1}$, via (14);
Update $\mathbf{I}_{j+1}$, via (17);
Update $\mathbf{S}_{j+1}$, via (19);
Update parameters $\alpha'_{j+1}=r*\alpha'_j$, $\beta'_{j+1}=r*\beta'_j$;
End While
OUTPUT: The sharp corrected image $\mathbf{I}$.

III. Experimental Results

A. Comparisons With State-of-The-Arts Methods

To demonstrate the superiority of the proposed method, we compare it with the state-of-the-arts methods, including gradient-filtering (GF) method [5], [6], nonuniformity correction via ℓ_0-regularized prior (NUCℓ_0) [17], nonuniformity correction using the global and local sparsity constraints (GLSC) [19], nonuniformity correction via single-frame and inter-frame structural similarity (NUCSS) [34], aerothermal radiation correction based on cyclic multiscale illumination self-similarity and gradient perception regularization (CMISGP) [18], thermal bias correction using Huber function-based loss (HFL) [9]. We name the proposed method NUCOSℓ_0 for short.

B. Subjective Assessment

1) Remote Sensing Images With Nonuniformity Effects: An IR scene of a city area shown in Fig. 3(a) is degraded by optics nonuniformity effects. Obviously, the intensities at the center of Fig. 3(a) is higher than ones at the corners. The corrected images are shown in Fig. 3(b)–(h), and the corresponding estimated thermal biases are located at the southeast corners. After correction, the resulting images in Fig. 3(c), (d), and (h) have a flatter background, which means that their correction residual errors are relatively smaller. The dark area on the right side of Fig. 3(b) and (g) has lower intensities, which means that their correction residual errors are larger. The thermal biases estimated by NUCSS and CMISGP are not smooth in Fig. 3(e) and (f), and thus their estimation errors are larger. Meanwhile, image structures are not well preserved by CMISGP in Fig. 3(f).

Another IR scene of a bridge over a river is also degraded by the same kind of nonunifomity effects in Fig. 4(a). If the river surface is observed in Fig. 4, NUCOSℓ_0 has so smaller correction error that the river surface in Fig. 4(h) is relatively flatter and image contrast between the river surface and the river bank is better preserved. Since the correction performance of GF, NUCℓ_0, and GLSC is affected by large-scale image structures, such as bridge, their correction errors are larger especially along the bridge in Fig. 4(b)–(d). The correction errors of NUCSS and CMISGP are also higher because the estimated thermal biases are not smooth in Fig. 4(e) and (f). The uneven river surface in Fig. 4(g) shows that HFL has a relatively large correction residual error.

2) Degraded IR Images With Partially Saturated Pixels: IR bush with partially saturated pixels shown in Fig. 5(a) is salient. To balance the intensity information and make the dim target in the sky easily be detected, the different methods are used to correct it, and their resulting images are shown in Fig. 5(b)–(h). For the region of the sky, CMISGP, HFL, and NUCOSℓ_0 have

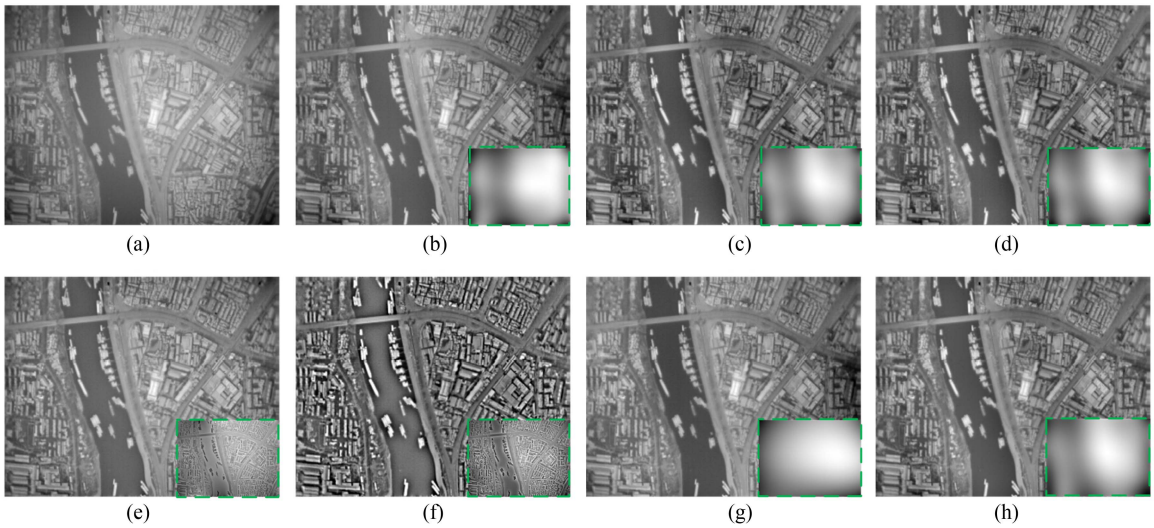


Fig. 3. (a) IR degraded image, (b) GF, (c) NUCℓ_0, (d) GLSC, (e) NUCSS, (f) CMISGP, (g) HFL, and (h) NUCOSℓ_0.

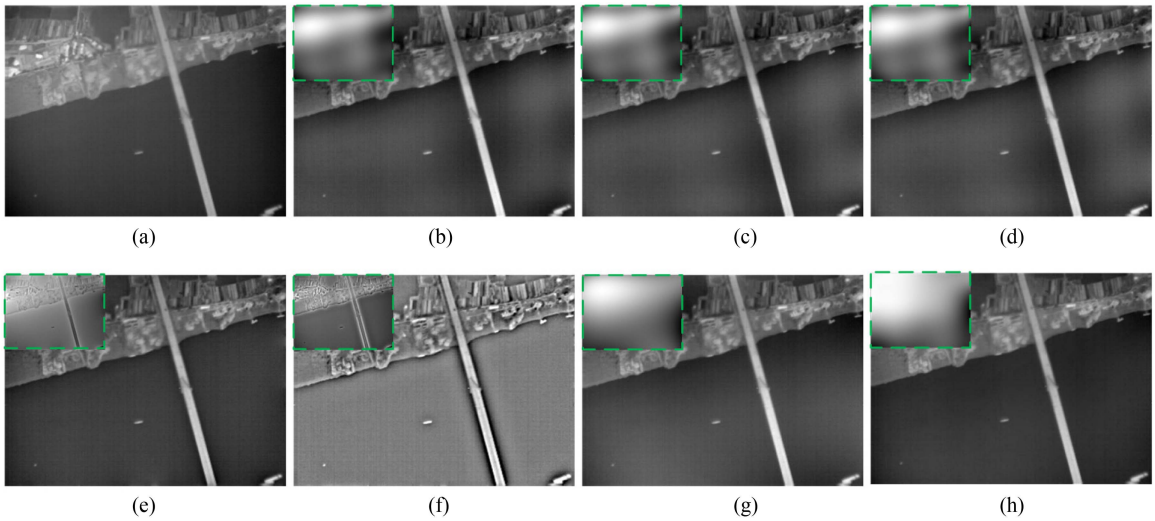


Fig. 4. (a) IR degraded image, (b) GF, (c) NUCℓ_0, (d) GLSC, (e) NUCSS, (f) CMISGP, (g) HFL, and (h) NUCOSℓ_0.

a relatively even background in Fig. 5(f), (g), and (h). However, CMISGP does not well preserve image contrast between the bushes and the sky in Fig. 5(f) and HFL cannot accurately estimate the thermal bias from the bushes with high intensities in Fig. 5(g). NUCOSℓ_0 not only effectively maintains image contrast, but also accurately estimates the thermal bias from the bushes in Fig. 5(h). Among all the comparative methods, NUCSS and CMISGP cannot well compute the thermal bias and have the larger residuals in Fig. 5(e) and (f). It is much challenging not only to effectively estimate the thermal bias from partially saturated Fig. 6(a), but also to well maintain the detail characteristics. If the estimated thermal biases are compared in Fig. 6(b)–(h), it can be easily observed in Fig. 6(g) and (h) that HFL and NUCOSℓ_0 have much higher estimation precision, whose biases gradually and smoothly decrease from the bottom to the top. If the regions of the sky background are compared further, NUCOSℓ_0 makes the sky background flatter, and thus the resulting image in Fig. 6(h) looks more natural.

3) IR Images Degraded by Outer Heat Sources: The nonuniformity effects in Fig. 7(a) are induced by the stray IR light from an outer heat source. Most of the comparative methods can so effectively estimate the nonuniformity background that the resulting images have sharp detail characteristics in Fig. 7(b)–(d), (g), and (h) except NUCSS and CMISGP. For example, the cumulus clouds in the sky in the above resulting images have the clear outlines. Contrarily, NUCSS and CMISGP produce larger estimation residual errors in Fig. 7(e) and (f). If the regions of the sky are zoomed in, it can be observed that NUCℓ_0 and NUCOSℓ_0 have the excellent ability of simultaneous nonuniformity correction and noise suppression in Fig. 7(c) and (h). Thanks to the introduction of second-order ℓ_0 sparsity, NUCOSℓ_0 successfully removes the staircase effects in the region of the sky in Fig. 7(h). The same nonuniformity effects can be also observed in Fig. 8(a). If all the estimated thermal biases are compared, most of the comparative methods have the relatively small correction residual errors except NUCSS and

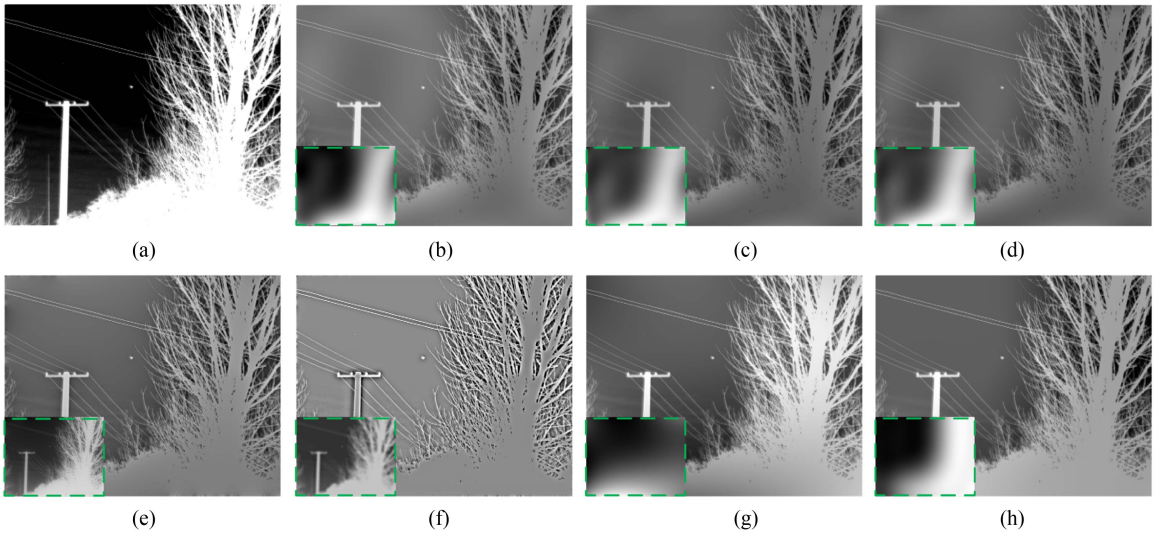


Fig. 5. (a) IR degraded image, (b) GF, (c) NUCℓ_0, (d) GLSC, (e) NUCSS, (f) CMISGP, (g) HFL, and (h) NUCOSℓ_0.

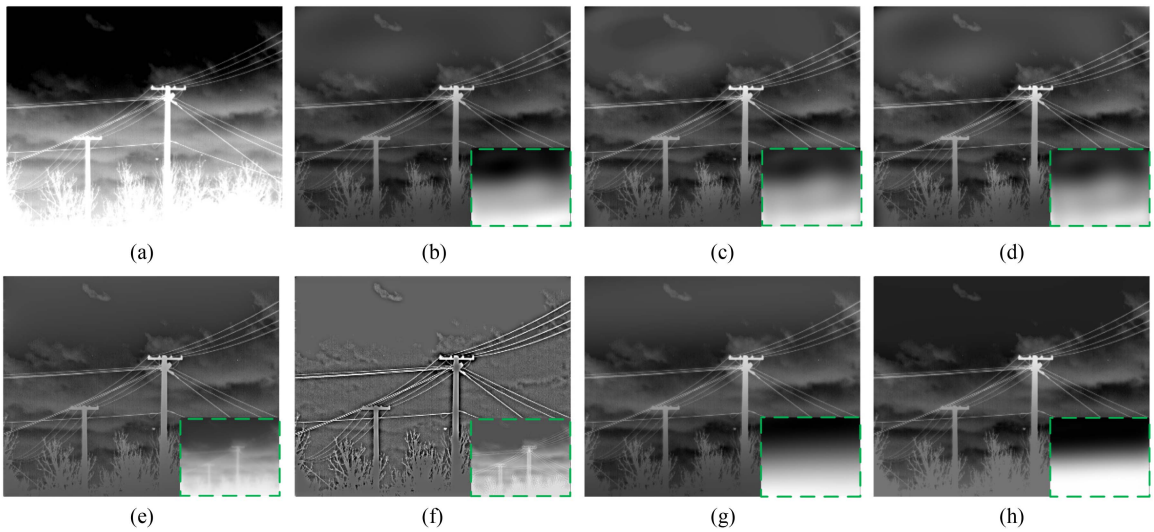


Fig. 6. (a) IR degraded image, (b) GF, (c) NUCℓ_0, (d) GLSC, (e) NUCSS, (f) CMISGP, (g) HFL, and (h) NUCOSℓ_0.

CMISGP. Among them, NUCOSℓ_0 can simultaneously preserve image detail characteristics and suppress system noise without producing staircase effects in the region of sky in Fig. 8(h).

4) Sea–Sky Line Images Degraded by Complex Nonuniformity and Partially Saturated Pixels: An IR scene of sea–sky line shown in Fig. 9(a) is degraded by complex nonuniformity and partially saturated pixels in the left most column. It is not easy to well preserve the sea–sky line with high contrast while removing the complex thermal bias. Both GF and HFL induce the periodic interference in Fig. 9(b) and (g) due to the intertwined impact of thermal bias and partially saturated pixels. NUCℓ_0, GLSC, and NUCOSℓ_0 can successfully estimate the complex thermal bias in Fig. 9(c), (d), and (h). Among them, NUCOSℓ_0 better preserves high contrast near the sea–sky line, and the region of the sky in Fig. 9(h) is much flatter. Another IR scene of a sea–sky line shown in Fig. 10(a) contains a large-scale thermal bias. If the estimated thermal biases are compared, HFL and NUCOSℓ_0 have the lower correction errors because the estimated thermal biases are not affected by the sea–sky line in Fig. 10(g) and (h). As the regions of the sky are observed, NUCOSℓ_0 successfully suppresses the noise in Fig. 10(h).

5) Experimental IR Images Degraded by Optics Temperature-Dependent Nonuniformity: The experimental IR image in Fig. 11(a) is degraded by the optics temperature-dependent nonuniformity effects. Since the resulting images in Fig. 11(c) and (h) have the lowest correction residual errors, their backgrounds are more flatter and their details are sharper. Obviously, NUCOSℓ_0 so successfully removes the staircase effects of image background that the resulting image in Fig. 11(h) looks natural. As the experiment temperature increases, the adverse nonuniformity effects are more severe in Fig. 12(a). The comparison of different resulting images demonstrates that NUCOSℓ_0 can not only accurately estimate the thermal bias, but

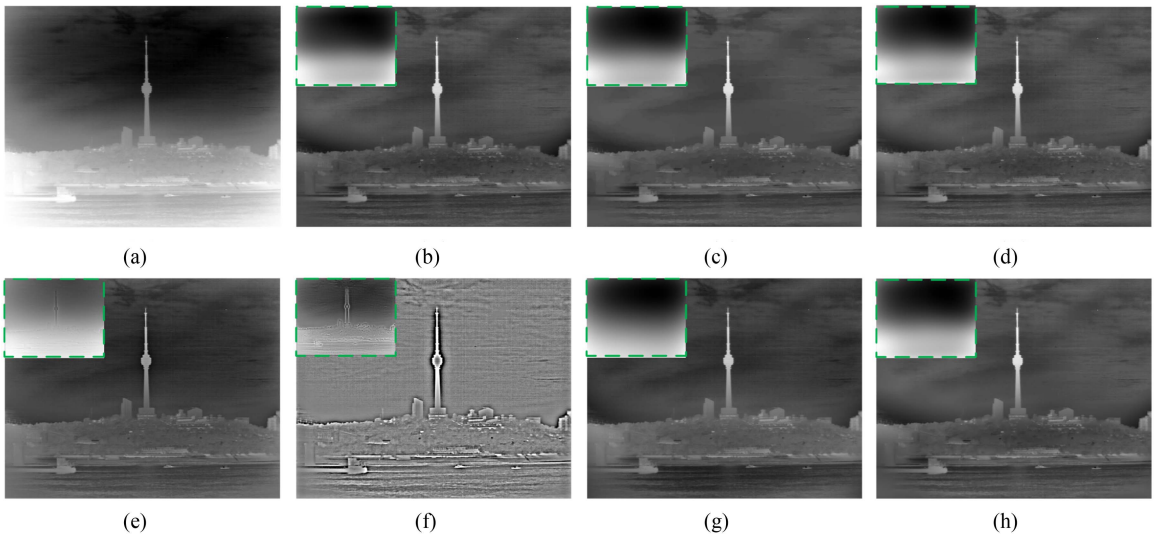


Fig. 7. (a) IR degraded image, (b) GF, (c) NUCℓ_0, (d) GLSC, (e) NUCSS, (f) CMISGP, (g) HFL, and (h) NUCOSℓ_0.

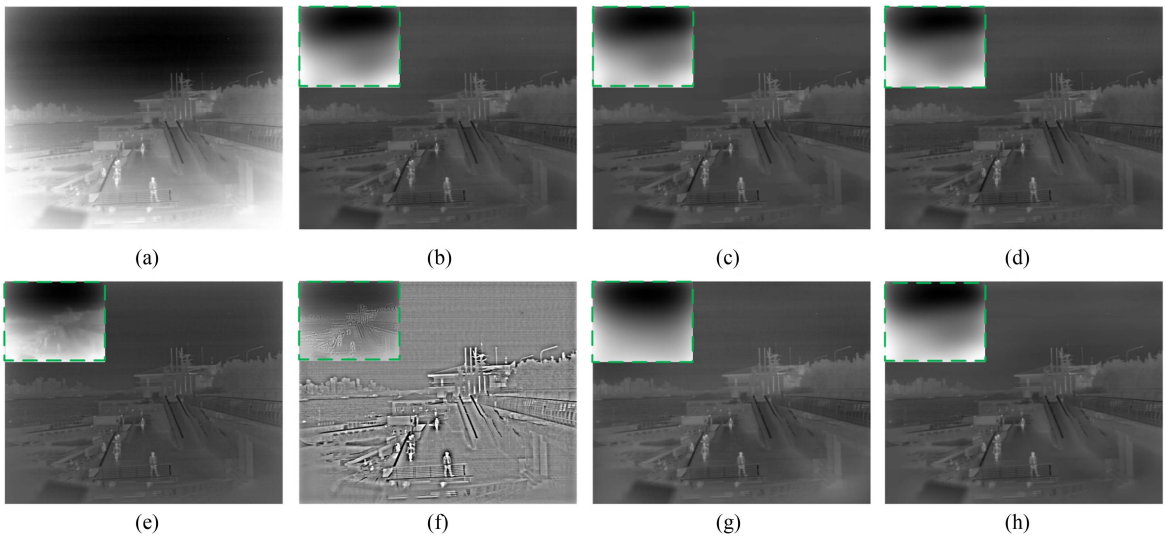


Fig. 8. (a) IR degraded image, (b) GF, (c) NUCℓ_0, (d) GLSC, (e) NUCSS, (f) CMISGP, (g) HFL, and (h) NUCOSℓ_0.

also remove the random noise without inducing the unnatural staircase effects in Fig. 12(h).

C. Objective Assessment

It is not enough to fully assess all comparative methods only by subjective assessment. Since there are no reference images in real-world datasets, we introduce the coefficient of variation (CV) and the standard deviation of image noise (σ_c) to quantitatively evaluate the effectiveness of the proposed method on real-world images. The former can be used to measure the roughness of corrected image, and the latter can be applied to estimate the noise level in a corrected image. The larger the value of CV is, the flatter the background of image is

$$\mathrm{CV} = \frac{\sigma(\mathbf{I})}{\mu(\mathbf{I})} \neq \frac{\sigma(\mathbf{I}+\delta)}{\mu(\mathbf{I}+\delta)} = \frac{\sigma(\mathbf{I})}{\mu(\mathbf{I})+\delta} \tag{20}$$

where σ and μ denote the standard deviation and mean value of the corrected image I, respectively. The value of CV is not invariant to the translation transformation. In specific, if δ is the increment of pixel intensity, the value of CV varies with the mean value of the corrected image. Thus, to effectively compute it, the mean value in (20) is same in each case for all comparative methods.

The estimated noise σ_c using the robust median estimator [35] is given in as

$$\sigma_c = \frac{\mathrm{Median}(|W_{HH}|)}{0.6745} \tag{21}$$

where W_{HH} is the set of wavelet coefficients of the corrected image in the smallest subband with diagonal direction.

It can be found in Tables I and II that NUCOSℓ_0 achieves the good performance indexes in most of experimental images, which means it cannot only effectively estimate the complex

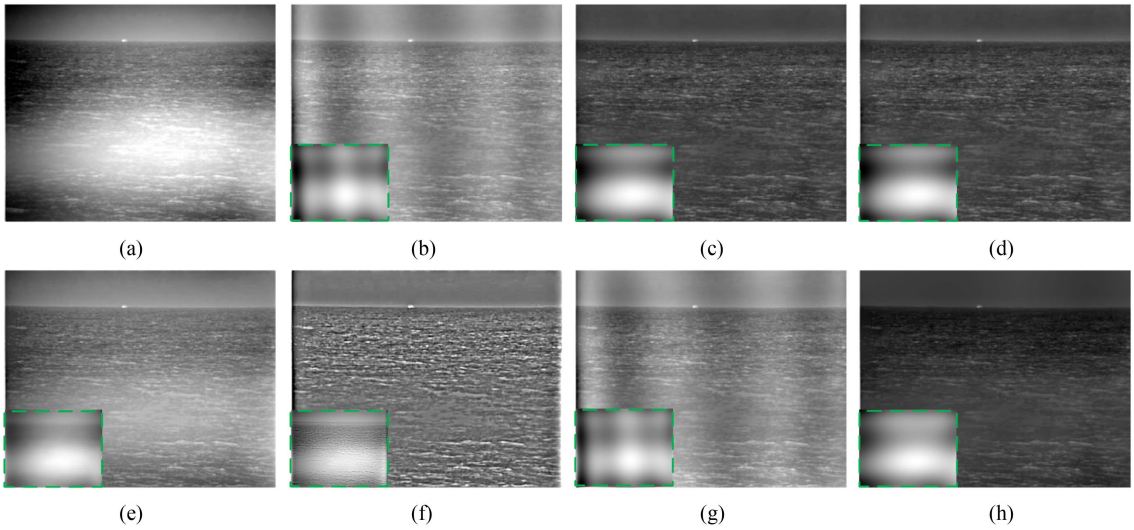


Fig. 9. (a) IR degraded image, (b) GF, (c) NUCℓ_0, (d) GLSC, (e) NUCSS, (f) CMISGP, (g) HFL, and (h) NUCOSℓ_0.

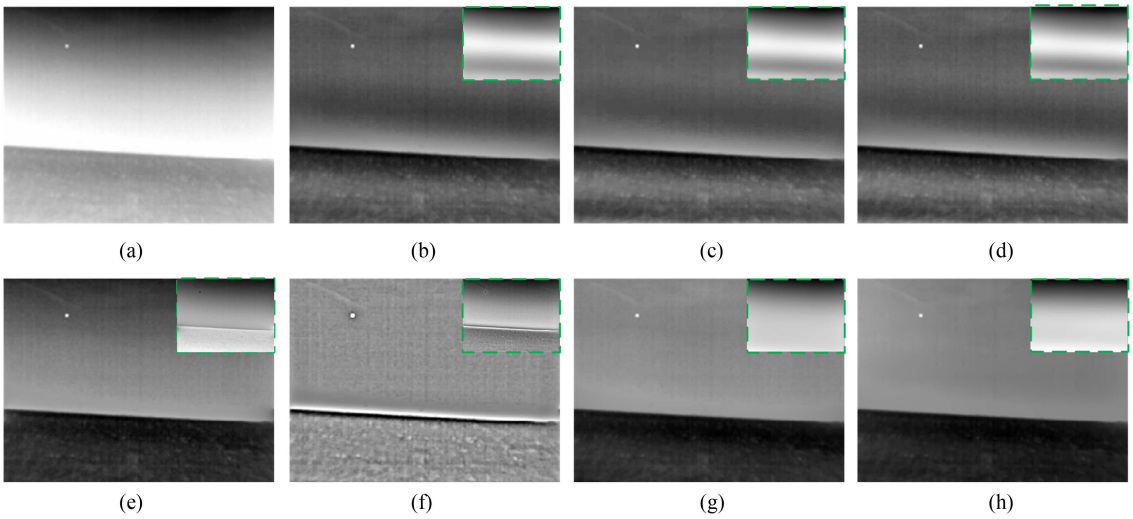


Fig. 10. (a) IR degraded image, (b) GF, (c) NUCℓ_0, (d) GLSC, (e) NUCSS, (f) CMISGP, (g) HFL, and (h) NUCOSℓ_0.

TABLE I
QUANTITATIVE COMPARISON OF PERFORMANCE INDEXES (CV AND σ_c) ON REAL-WORLD IR IMAGES

Method	Fig. 3		Fig. 4		Fig. 5		Fig. 6		Fig. 7	
	CV	σ_c	CV	σ_c	CV	σ_c	CV	σ_c	CV	σ_c
GF	0.014	57.213	**0.004**	13.267	0.322	1.597	0.139	1.296	0.080	1.881
NUCℓ_0	**0.010**	56.166	**0.004**	11.636	0.312	1.507	**0.138**	1.221	**0.072**	**0.513**
GLSC	**0.010**	55.884	**0.004**	12.887	0.310	1.566	0.310	1.566	0.076	1.652
NUCSS	0.017	88.405	0.006	21.435	0.262	1.171	0.262	1.171	0.201	3.177
CMISGP	0.025	198.995	0.006	38.780	**0.204**	1.801	0.204	1.801	0.209	11.827
HFL	0.014	57.327	0.005	13.349	0.530	1.610	0.158	1.282	0.132	1.897
NUCOSℓ_0	**0.010**	**55.108**	0.006	**7.028**	0.353	**0.492**	0.317	**0.994**	0.076	0.741

*The best value of the index is in bold.

thermal bias, but also well suppress the random noise from image acquisition. However, NUCOSℓ_0 does not have the best value of CV in Figs. 4–6, Fig. 9, and Fig. 10. These degraded images all have the salient image structure with high contrast, such as the noticeable border along the river bank in Fig. 4, the significant contrast between the partially saturated pixels and the dark sky in Fig. 6 and so on. If the significant image structures are well preserved, the CV values are relatively high. The central lines of normalized pixel intensities cropped from the abovementioned corrected images are shown in Fig. 13. It can be observed in

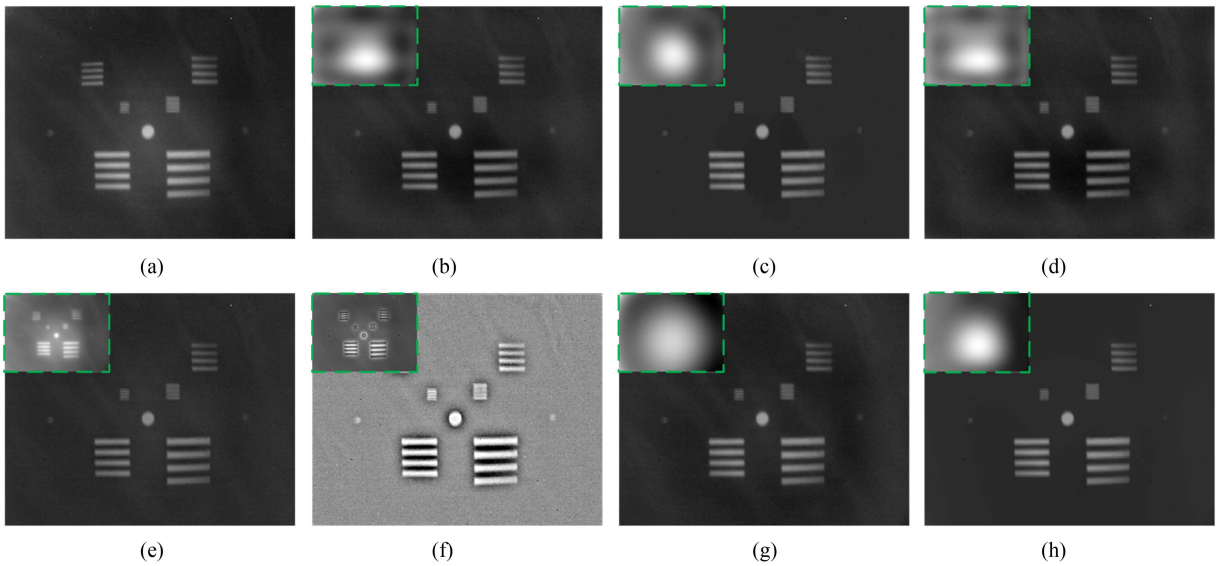


Fig. 11. (a) IR degraded image, (b) GF, (c) NUCℓ_0, (d) GLSC, (e) NUCSS, (f) CMISGP, (g) HFL, and (h) NUCOSℓ_0.

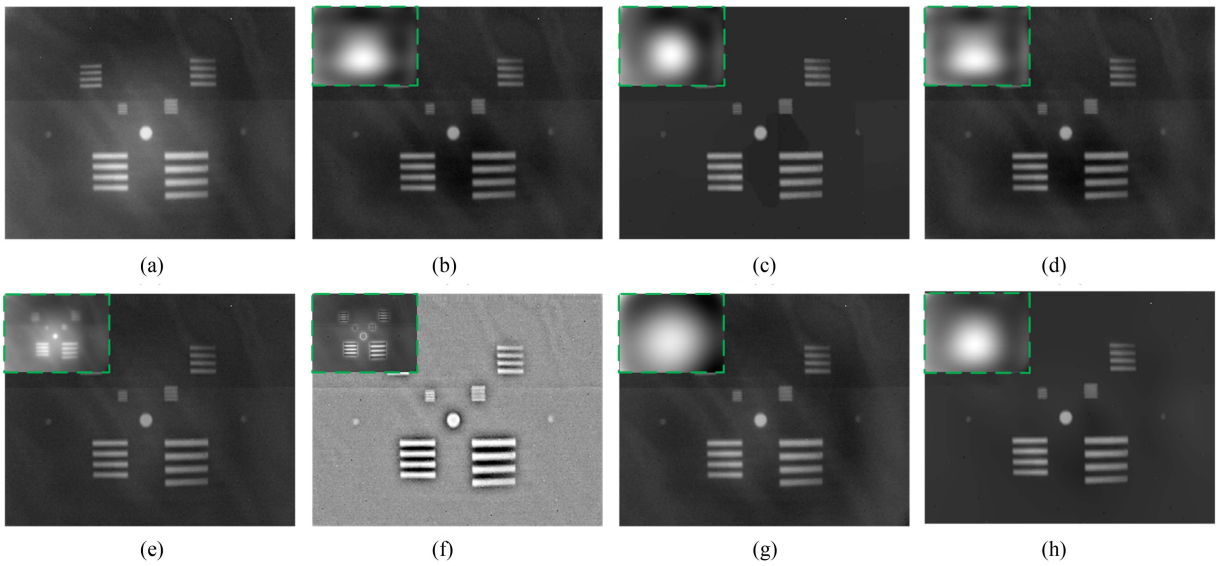


Fig. 12. (a) IR degraded image, (b) GF, (c) NUCℓ_0, (d) GLSC, (e) NUCSS, (f) CMISGP, (g) HFL, and (h) NUCOSℓ_0.

TABLE II
QUANTITATIVE COMPARISON OF PERFORMANCE INDEXES (CV AND σ_c) ON REAL-WORLD IR IMAGES

Method	Fig. 8		Fig. 9		Fig. 10		Fig. 11		Fig. 12	
	CV	σ_c	CV	σ_c	CV	σ_c	CV	σ_c	CV	σ_c
GF	0.070	1.775	0.154	3.537	0.084	0.535	0.148	2.850	0.127	3.089
NUCℓ_0	0.068	0.330	**0.081**	3.419	0.065	0.720	0.084	**0.000**	0.109	0.001
GLSC	**0.065**	1.587	0.082	3.494	**0.037**	0.556	0.149	2.643	0.125	2.822
NUCSS	0.059	1.688	0.234	3.935	0.157	0.982	0.102	2.740	0.122	3.103
CMISGP	0.143	9.139	0.202	10.026	0.059	2.023	0.725	8.008	0.352	8.051
HFL	0.099	1.801	0.329	3.593	0.249	0.562	0.160	2.866	0.159	3.095
NUCOSℓ_0	0.066	**0.234**	0.118	**3.200**	0.258	**0.092**	**0.081**	**0.000**	**0.102**	**0.000**

*The best value of the index is in bold.

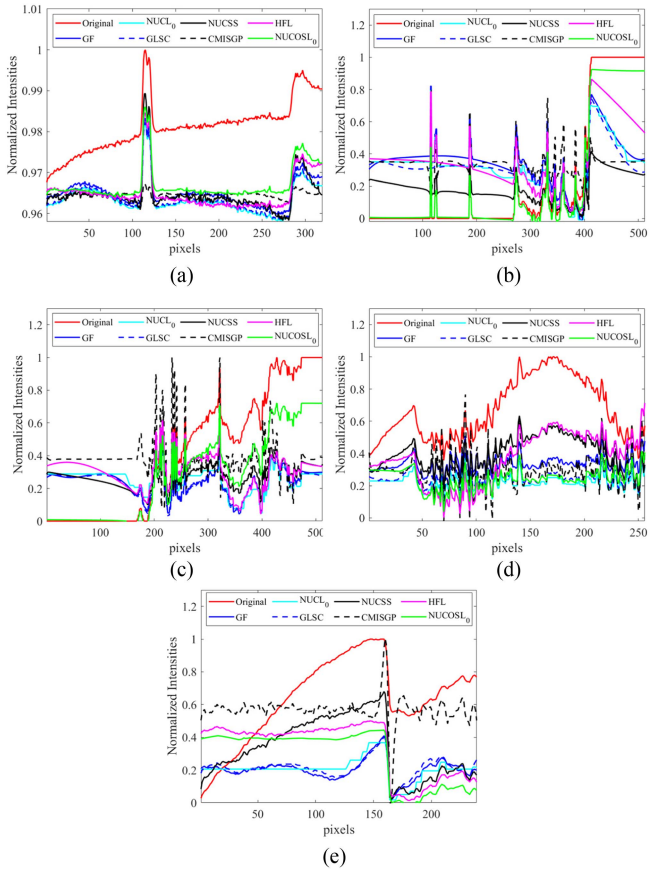


Fig. 13. (a)–(e) Normalized intensities of the central column of Figs. 4–6, Fig. 9, and Fig. 10.

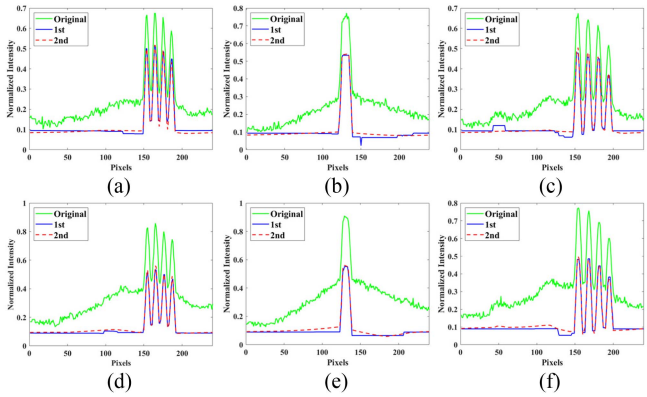


Fig. 14. Comparative results of the correction model with the first- and second-order ℓ_0 sparsity. (a)–(c) Three columns of normalized pixel values cropped from Fig. 11. (d)–(f) Three columns of normalized pixel values cropped from Fig. 12.

TABLE III
QUANTITATIVE COMPARISON OF PERFORMANCE INDEXES (CV AND σ_c) ON CONSECUTIVE 100 FRAMES OF EXPERIMENTAL IMAGES

Methods	First 50 Frames		Second 50 Frames	
	CV	σ_c	CV	σ_c
NUCℓ_0	0.0222	2.95e-05	0.0444	2.50e-04
NUCℓ_0S	0.0283	4.12e-06	0.0454	1.25e-04
NUCOSℓ_0	0.0213	4.22e-07	0.0380	7.07e-05

Fig. 13 that although the CV values of the abovementioned corrected images are higher, NUCOSℓ_0 can more effectively preserve salient image structures while removing thermal bias. The great advantage of NUCOSℓ_0 can be also verified that simultaneous thermal bias estimation and noise suppression has been so successfully achieved in a unified correction framework that the resulting images have friendly visual quality and lowest residual errors, especially in Figs. 11 and 12.

D. Parameter Selection

There are three important parameters α, β, and K in the proposed model. The parameter α has a crucial role in controlling the estimation precision of thermal bias especially in degraded images with high-contrast structures and the parameter β can not only have a significant impact on the estimation precision, but also reduce the noise level of the resulting images. In this study, α and β are set empirically in the range [10, 200] and [1, 10], respectively. The order K has a direct impact on the estimated thermal bias, and its optimal value has been investigated in the previous study [19]. Thus, K is set to 8 in all cases. Finally, since the penalty parameters α' and β' do not greatly affect the convergence, which are empirically set until the resulting image obtained the best quality.

E. Ablation Study

The proposed correction method is optimized in two aspects, not only to improve estimation precision of thermal bias but also to preserve significant image characteristics. On the one hand, the second term in (7) aims to improve estimation accuracy by limiting the adverse impact of both outliers and large-scale image structures on thermal bias. For example, how to accurately estimate the thermal bias from Fig. 9(a) and Fig. 10(a) and effectively preserve the sea–sky line is much challenging. Since the successful outliers handling schemes is well designed, the estimation precision is significantly improved especially for severely degraded images with complex nonuniformity and salient structures.

On the other hand, compared to the traditional ℓ_0 norm regularization, the second-order ℓ_0 norm sparsity in gradient domain can so effectively restrain the staircase effects that the estimation precision of thermal bias is improved further. Meanwhile, it can significantly penalize noise while preserving image structures. The comparative results of the proposed correction method with the first- and second-order regularization term, respectively, are shown in Fig. 14. Obviously, the staircase effects are significantly reduced due to the introduction of the second-order ℓ_0 norm sparsity in (7). In addition, the correction model with first-order ℓ_0 norm regularization (NUCℓ_0), one with second-order norm regularization (NUCℓ_0S), and the proposed method perform the consecutive 100 frames of experimental IR images where the nonuniformity effects become more and more severe. The quantitative results are shown in Table III. In the whole experimental image sequence, the proposed

method have the better correction performance in terms of CV and σ_c.

IV. Conclusion

The great advantage of the proposed method is to simultaneously estimate thermal bias from the severely degraded image and suppress system noise in a unified correction framework. The proposed model is optimized from two intertwined aspects. On the one hand, an effective outlier handling scheme is made to improve the estimation precision of thermal bias especially for degraded images with complex bias and salient structures. On the other hand, the second-order ℓ_0 norm sparsity in gradient domain is well designed not only to improve the estimation precision further, but also to remove system noise while preserving the significant detail characteristics. The above optimization strategy is successfully implemented to produce a high-quality corrected image.

It is not easy to achieve a successful learning-based correction model to effectively address IR nonuniformity issue due to both the complexity of the real-world degradation process and the variation of IR scenes. In the future, combining physics-based models and deep learning can further improve the effectiveness and efficiency of the correction model.

Acknowledgment

The related experiment data and code can be obtained by request.

References

[1] N. Oz, N. Sochen, D. Mendlovic, and I. Klapp, "Estimating temperatures with low-cost infrared cameras using physically-constrained deep neural networks," *Opt. Exp.*, vol. 32, pp. 30565–30582, 2024.

[2] W. Hui et al., "Evaluating imaging quality of optical dome affected by aero-optical transmission effect and aero-thermal radiation effect," *Opt. Exp.*, vol. 28, pp. 6172–6187, 2020.

[3] A. D. Restrepo-Girón and H. Loaiza-Correa, "Background thermal compensation by filtering for contrast enhancement in active thermography," *J. Nondestruct Eval.*, vol. 35, no. 20, 2016, Art. no. 20.

[4] Y. Zhang et al., "Effect of background subtraction on defect detection in thermographic signal reconstruction coefficient images," *J. Nondestruct Eval.*, vol. 41, no. 44, 2022, Art. no. 44.

[5] Y. Cao and C. L. Tisse, "Single-image-based solution for optics temperature-dependent nonuniformity correction in an uncooled longwave infrared camera," *Opt. Lett.*, vol. 39, no. 3, pp. 646–648, Feb. 2014.

[6] Y. Li, W. Jin, and Z. Liu, "Interior radiation noise reduction method based on multiframe processing in infrared focal plane arrays imaging system," *IEEE Photon. J.*, vol. 10 no. 5, Oct. 2018, Art. no. 6803512.

[7] Y. Shi, J. Chen, H. Hong, Y. Zhang, N. Sang, and T. Zhang, "Multi-scale thermal radiation effects correction via a fast surface fitting with Chebyshev polynomials," *Appl. Opt*, vol. 61, pp. 7498–7507, 2022.

[8] H. Hong, J. Liu, Y. Shi, L. Xiong, N. Sang, and T. Zhang, "Progressive nonuniformity correction for aero-optical thermal radiation images via bilateral filtering and Bézier surface fitting," *IEEE Photon. J.*, vol. 15, no. 2, Apr. 2023, Art. no. 7800611.

[9] J. Xie, L. Song, and H. Huang, "Thermal radiation bias correction for infrared images using Huber function-based loss," *IEEE Trans. Geosci. Remote Sens.*, vol. 62, 2024, Art. no. 5002115.

[10] T. Liu et al., "Enhanced gradient-domain LMS method for bias field correction in infrared images," *Opt. Laser Technol.*, vol. 169, 2024, Art. no. 110148.

[11] Y. Chang, L. Yan, L. Liu, H. Fang, and S. Zhong, "Infrared aerothermal nonuniform correction via deep multiscale residual network," *IEEE Geosci. Remote Sens. Lett.*, vol. 16, no. 7, pp. 1120–1124, Jul. 2019.

[12] Y. Shi, X. Deng, L. Wang, Y. Zhang, and Z. Huang, "Semi-supervised learning for infrared thermal radiation correction in the real world," *IEEE Trans. Geosci. Remote Sens.*, vol. 62, 2024, Art. no. 5007114.

[13] Y. Shi, S. Niu, L. Wang, L. Ye, Y. Zhang, and H. Hong, "SFMHANet: Surface fitting constrained multidimensional hybrid attention network for aero-optics thermal radiation effect correction," *IEEE J. Sel. Topics Appl. Earth Observ. Remote Sens.*, vol. 18, pp. 4568–4583, 2025.

[14] H. Fang et al., "Detection-friendly nonuniformity correction: A union framework for infrared UAV target detection," in *Proc. IEEE Conf. Comput. Vis. Pattern Recognit.*, Nashville, TN, USA, Jun. 2025, pp. 11898–11907.

[15] V. Saragadam, A. Dave, A. Veeraraghavan, and R. G. Baraniuk, "Thermal image processing via physics-inspired deep networks," in *Proc. IEEE/CVF Int. Conf. Comput. Vis. Workshops*, Montreal, BC, Canada, 2021, pp. 4040–4048.

[16] X. Ren, W. Yang, W. H. Cheng, and J. Liu, "LR3M: Robust low-light enhancement via low-rank regularized retinex model," *IEEE Trans. Image Process.*, vol. 29, pp. 5862–5876, Apr. 2020.

[17] L. Liu and T. Zhang, "Optics temperature-dependent nonuniformity correction via ℓ_0-Regularized prior for airborne infrared imaging systems," *IEEE Photon. J.*, vol. 8, no. 5, pp. 1–10, Oct. 2016.

[18] Y. Wang, X. Sui, Y. Wang, T. Liu, C. Zhang, and Q. Chen, "Contrast enhancement method in aero thermal radiation images based on cyclic multi-scale illumination self-similarity and gradient perception regularization," *Opt. Exp.*, vol. 32, pp. 1650–1668, 2024.

[19] L. Liu, L. Xu, and H. Fang, "Simultaneous intensity bias estimation and stripe noise removal in infrared images using the global and local sparsity constraints," *IEEE Trans. Geosci. Remote Sens.*, vol. 58, no. 3, pp. 1777–1789, Mar. 2020.

[20] Y. Liu, B. Qiu, Y. Tian, J. Cai, X. Sui, and Q. Chen, "Scene-based dual domain non-uniformity correction algorithm for stripe and optics-caused fixed pattern noise removal," *Opt. Exp.*, vol. 32, pp. 16591–16610, 2024.

[21] Y. He, C. Zhang, B. Zhang, and Z. Chen, "FSPnP: Plug-and-play frequency–spatial-domain hybrid denoiser for thermal infrared image," *IEEE Trans. Geosci. Remote Sens.*, vol. 62, pp. 1–16, 2024.

[22] X. Zhang, R. Wang, D. Chen, Y. Zhao, and W. Gao, "Handling outliers by robust m-estimation in blind image deblurring," *IEEE Trans. Multimedia*, vol. 23, pp. 3215–3226, 2021.

[23] H. Y. Shu, Y. H. Lin, and Y. C. Lu, "Deep plug-and-play nighttime non-blind deblurring with saturated pixel handling schemes," in *Proc. IEEE/CVF Winter Conf. App. Comput. Vis.*, Waikoloa, HI, USA, 2024, pp. 1527–1535.

[24] Y. Shi, Y. Zhou, L. Ma, L. Wang, and H. Hong, "WDTSNet: Wavelet decomposition two-stage network for infrared thermal radiation effect correction," *IEEE Trans. Geosci. Remote Sens.*, vol. 62, 2024, Art. no. 5609917.

[25] D. Zhang, J. He, Y. Zhou, D. Chen, and Z. Wang, "Hybrid low-rank and sparsity constraint with Hankel structure preservation for simultaneous seismic reconstruction and denoising," *IEEE Geosci. Remote Sens. Lett.*, vol. 20, 2023, Art. no. 7502105.

[26] G. Xu et al., "A robust nonlocal tensor decomposition method for inSAR phase denoising," *IEEE Trans. Geosci. Remote Sens.*, vol. 62, 2024, Art. no. 5216511.

[27] X. Fu, Y. Guo, M. Xu, and S. Jia, "Hyperspectral image denoising via robust subspace estimation and group sparsity constraint," *IEEE Trans. Geosci. Remote Sens.*, vol. 61, 2023, Art. no. 5512716.

[28] G. Hou, N. Li, P. Zhuang, K. Li, H. Sun, and C. Li, "Non-uniform illumination underwater image restoration via illumination channel sparsity prior," *IEEE Trans. Circuits Syst. Video Technol.*, vol. 34, no. 2, pp. 799–814, Feb. 2024.

[29] Z. Wang, Y. Guo, W. Kang, and X. Chen, "A novel fault feature extraction method for planet-bearing based on generalized total variation model," *IEEE Sensors J.*, vol. 25, no. 11, pp. 20870–20879, Jun. 2025.

[30] X. Liu and W. Lian, "Non-convex high-order TV and ℓ0-Norm wavelet frame-based speckle noise reduction," *IEEE Trans. Circuits Syst. II, Exp. Briefs*, vol. 69, no. 12, pp. 5174–5178, Dec. 2022.

[31] H. Wang and S. Yu, "Regularized full-waveform inversion with Shearlet transform and total generalized variation," *IEEE Trans. Geosci. Remote Sens.*, vol. 62, 2024, Art. no. 5925115.

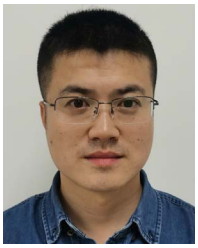
[32] S. Takemoto, K. Naganuma, and S. Ono, "Spatio-spectral structure tensor total variation for hyperspectral image denoising and destriping," *IEEE J. Sel. Topics Appl. Earth Observ. Remote Sens.*, vol. 18, pp. 19157–19175, 2025.

[33] J. Pan, Z. Hu, Z. Su, and M. H. Yang, " L_0-regularized intensity and gradient prior for deblurring text images and beyond," *IEEE Trans. Pattern Anal. Mach. Intell.*, vol. 39, no. 2, pp. 342–355, Feb. 2017.
[34] Y. Wang, Y. Wang, T. Liu, X. Sui, G. Gu, and Q. Chen, "Enhancing infrared imaging systems with temperature-dependent nonuniformity correction via single-frame and inter-frame structural similarity," *Appl. Opt.*, vol. 62, pp. 7075–7082, 2023.
[35] B. G. Jeong, B. C. Kim, Y. H. Moon, and I. K. Eom, "Simplified noise model parameter estimation for signal-dependent noise," *Signal Process.*, vol. 96, pp. 266–273, Mar. 2014.



Li Liu (Member, IEEE) received the Ph.D. degree in control science and technology from the Huazhong University of Science and Technology, Wuhan, China, in 2016.

He is currently an Associate Professor with the School of Aerospace Science and Technology, Xidian University, Xian, China. From 2021 to 2023, he was a Postdoctoral Researcher with the University of Helsinki, Helsinki, Finland, funded by the China Scholarship Council (CSC). His main research interests include infrared image correction, image deblurring, image enhancement, and object detection and recognition.



Ji Liu received the M.S. degree in communication engineering from the University of Electronic Science and Technology of China, Chengdu, China, in 2013.

He is a Senior Researcher with the China Academy of Space Technology, Xi'an, China. His main research interests include hyperspectral image processing and signal processing.

Xinchao Zhang received the M.S. degree in communication engineering from the University of Electronic Science and Technology of China, Chengdu, China, in 2016.

He is a Senior Researcher with the National Key Laboratory of Air-based Information Perception and Fusion, Luoyang, China. His main research interests include target detection and image processing.

Weihua Meng received the Ph.D. degree in optics engineering from the Beijing Institute of Technology, Beijing, China, in 2010.

He is a Senior Researcher with the National Key Laboratory of Air-based Information Perception and Fusion, Luoyang, China. His main research interests include target detection, deep leaning, and image processing.



Houzhang Fang (Member, IEEE) received the Ph.D. degree in control science and engineering from the Huazhong University of Science and Technology, Wuhan, China, in 2014.

He is currently an Associate Professor with the School of Computer Science and Technology, Xidian University, Xi'an, China. His research interests include target recognition, target tracking, and image restoration.